

Diffeomorphic Cortical Alignment via Direct Warping of Streamline Endpoints

Yang Xiang¹, Martin Cole² and Zhengwu Zhang^{1,*}

¹ Department of Statistics and Operations Research, The University of North Carolina at Chapel Hill; xya@unc.edu

² Department of Psychiatry, University of Rochester; Martin_Cole@URMC.Rochester.edu

* Correspondence: zhengwu_zhang@unc.edu

Abstract

Cortical surface registration is often driven by local geometric descriptors (e.g., sulcal depth and curvature). While this approach achieves geometric correspondence, it neglects the long-range wiring constraints imposed by white-matter anatomy. Diffusion MRI tractography offers these crucial constraints; however, prior connectivity-informed pipelines typically align precomputed connectivity matrices, making the optimization highly sensitive to connectivity estimation and its resolution. In this paper, we introduce a novel connectivity-based surface registration method that aligns cortical surfaces by operating directly on white-matter fiber-tract endpoints. We model tract endpoints as a point cloud on the product manifold $\Omega \times \Omega$, where Ω represents the spherical domain of the inflated cortical hemispheres. Our alignment method iteratively (i) computes a small diffeomorphic warp for Ω by minimizing connectivity mismatch, and (ii) updates the endpoints based on this warp. The method relies on a geometric framework that ensures output warps are diffeomorphisms and has a final goal that optimizes the matching of well-known fiber bundles. Experiments on Human Connectome Project (HCP) data demonstrate improved tract-level correspondence, achieving higher connectivity-level overlap coefficients on major fiber bundles and stronger robustness across grid resolutions for Ω compared to state-of-the-art methods such as ENCORE and MSMAII.

Keywords: Cortical Surface Alignment; Brain Connectivity; Streamline Endpoints; Diffeomorphic Registration; Spherical Heat Kernel.

1. Introduction

Brain cortical surface registration is essential for establishing accurate point-to-point anatomical correspondence across subjects, a fundamental prerequisite for group-level neuroimaging and neuroscience studies (Fischl et al., 1999). Traditionally, inter-subject alignment is driven by local features derived from cortical folding geometry, such as sulcal depth and curvature (Fischl et al., 1999; Yeo et al., 2009; Robinson et al., 2014). However, local geometry exhibits immense inter-subject variability, particularly in the association cortex, and frequently fails to align structurally or functionally homologous regions (Glasser et al., 2016). Consequently, there is a growing need to incorporate supplementary anatomical priors to guide cortical surface registration.

Structural connectivity (SC) derived from diffusion MRI (dMRI) tractography offers a powerful, biologically grounded alternative (Cole et al., 2025). While local geometric descriptors can be confined to superficial topography, dMRI tractography reconstructs white-matter streamlines that map the physical, long-range pathways linking spatially distant cortical regions (see some examples in Figure 1(A)). Because these connections are heavily constrained by neurodevelopmental and foundational anatomical principles, they remain comparatively stable across individuals and times (Jbabdi et al., 2015; Osmanlıoğlu et al., 2020). By acting as robust, long-range anatomical anchors, SC features can disambiguate regions with similar folding patterns but distinct connectivity profiles, thereby significantly improving the alignment of corresponding cortical areas.

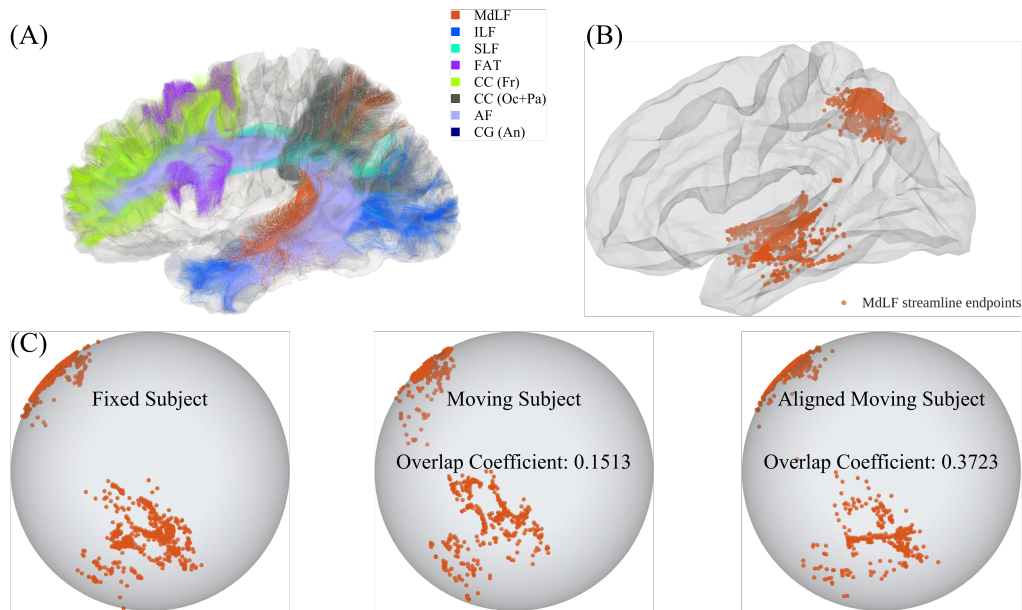


Figure 1. (A) Major streamlines on the cortical white surface. (B) Endpoints of streamlines from the Middle Longitudinal Fasciculus (MdLF) on the cortical white surface. (C): **Left:** Endpoints from (B) mapped to the spherical domain S^2 , serving as the fixed subject (target). **Middle:** Endpoints from the moving subject (source) before registration. **Right:** Endpoints from the moving subject after alignment to the target using the proposed method. Note that the direct point-cloud formulation successfully registers the structural constraints without relying on grid-based discretization.

Despite its potential, leveraging SC for surface registration introduces significant methodological challenges. Many existing SC-driven methods perform alignment by converting streamlines into a discretized, precomputed connectivity matrix (Gutman et al., 2014; Zhou et al., 2026). This reliance on matrix representations makes the registration optimization highly sensitive to connectivity estimation and resolution. Coarse resolutions inherently obscure fine-scale connectivity patterns, whereas high-resolution ones suffer from extreme sparsity, numerical instability, and prohibitive computational costs. Alternatively, while recent continuous connectivity approaches offer a resolution-free formulation (Cole et al., 2025), they introduce their own computational bottlenecks. Iteratively warping a continuous, surface-based connectivity profile requires repeated spatial re-interpolation and the frequent computation of Jacobian determinants. These operations introduce numerical diffusion and accumulate errors over successive iterations, ultimately resulting in suboptimal alignment performance.

To overcome these fundamental limitations, we propose a novel surface registration framework that operates directly on the exact spatial endpoints of white-matter fiber tracts. We model the tract endpoints as a point cloud situated on the product manifold $\Omega \times \Omega$, where Ω denotes the spherical domain corresponding to the inflated cortical hemispheres. This representation naturally encodes both endpoint spatial distribution and connectivity pattern generated from streamlines (see Figure 1(C) left panel; Figure 1(B) shows the corresponding cortical surface and endpoints without inflation). Figure 1(C) illustrates the main problem studied in this paper: aligning fiber-bundle endpoints across subjects. For clarity, only the MdLF bundle is visualized. The left and middle panels show the MdLF endpoints for the target and moving subjects, respectively, while the right panel shows the endpoints after alignment of the moving subject. The overlap coefficient, which measures the overlap between the target and moving subjects' MdLF endpoints, is greatly improved after alignment. Importantly, the registration is performed using all streamline endpoints, not just those from the MdLF bundle; the figure displays only MdLF endpoints for visualization purposes. The proposed method alternates between two principal steps: (i) estimating a small diffeomorphic deformation of the domain Ω by directly minimizing an endpoint mismatch objective, and (ii) updating the physical streamline endpoints according to the newly estimated deformation field.

We summarize our main contributions as follows:

1. We design a hybrid registration framework that leverages a continuous density proxy to compute deformation gradients. This ensures the estimated transformation is a strict diffeomorphism, guaranteeing smooth, invertible, and topologically consistent alignment.
2. By applying these deformations directly to the discrete streamline endpoints rather than a grid, the method bypasses connectivity matrix construction entirely. This matrix-free approach eliminates numerical diffusion, rendering the algorithm inherently robust to discretization resolution.
3. Comprehensive evaluations on Human Connectome Project (HCP) data demonstrate that our approach achieves superior alignment accuracy compared to state-of-the-art methods (e.g., ENCORE in [Cole et al. \(2025\)](#), MSMAll in [Robinson et al. \(2014\)](#)), particularly in aligning major white-matter fiber bundles.

The remainder of this paper is organized as follows. In Section 2, we review existing work on cortical surface alignment. In Section 3, we present our endpoint-based method in detail, including the introduction of ConCon as a density proxy, the formulation for minimizing connectivity mismatch, and our direct update of streamline endpoints. Section 4 describes the evaluation framework and the discretization grid used in our implementation. In Section 5, we report simulation results demonstrating that our algorithm remains accurate under large deformations and is robust to grid resolution. Finally, in Section 6, we apply our method to the HCP dataset and evaluate its performance against state-of-the-art registration methods, demonstrating higher overlap scores for most major fiber bundles.

2. Related Work

Geometry and Multimodal Surface Alignment. Brain cortical surface alignment has been extensively investigated, with a variety of features proposed to establish inter-subject correspondence. Classical surface-based registration methods rely heavily on folding geometry, utilizing sulcal depth and curvature to provide stable descriptors of gyrification on the spherical representation of the cortex ([Fischl et al., 1999](#); [Yeo et al., 2009](#)). Beyond pure geometry, anatomical measures such as cortical thickness have been incorporated to better capture inter-individual variability ([Das et al., 2009](#)). More recently, multimodal registration frameworks have emerged to integrate complementary structural and functional information. A prominent example is the MSMAll approach ([Robinson et al., 2014](#); [Glasser et al., 2016](#)), widely utilized in the Human Connectome Project, which combines folding geometry with myelin-sensitive contrasts and resting-state functional connectivity in a unified spherical matching framework.

Connectivity-Driven Alignment. In recent years, structural connectivity estimated from dMRI tractography has attracted growing interest as a biologically informed constraint for registration and network alignment ([Lazar, 2010](#); [Milano et al., 2017](#); [Zhang et al., 2022](#)). Several studies have demonstrated that incorporating SC profiles, either at the vertex level or via specific white-matter bundles, yields more accurate alignment of functionally corresponding regions across subjects compared to purely geometric methods ([Gutman et al., 2014](#); [Zhang et al., 2016](#); [Cole et al., 2025](#); [Zhou et al., 2026](#)). By leveraging long-range connection data, these approaches provide supplementary constraints that can supersede ambiguous local geometry. However, because current pipelines rely heavily on pre-computed connectivity matrices, their optimization remains bottlenecked by grid resolution, matrix sparsity, and connectivity estimation accuracy ([Cole et al., 2025](#); [Zhou et al., 2026](#)).

Deep Learning for Registration. The rise of deep learning has introduced highly efficient alternative frameworks for brain registration, including volume-based methods like VoxelMorph ([Balakrishnan et al., 2019](#)) and various spherical CNN-based architectures for surface alignment ([Zhao et al., 2021](#); [Cheng et al., 2020](#); [Li et al., 2024](#)). While these deep learning models achieve substantially faster inference times than the iterative gradient-based framework proposed in this paper, they face distinct topological challenges. Specifically, neural networks typically rely on explicit regularization terms or highly specific architectural constraints (e.g., stationary velocity field integration) to encourage

smooth and invertible deformation fields. In contrast, our proposed geometric framework inherently guarantees strict diffeomorphic behavior and topological preservation by design, without the need for extensive hyperparameter tuning or post-hoc regularization.

3. Methodology

We present a connectivity-driven framework for cortical surface alignment based on streamline endpoints. Given streamline endpoints represented as discrete point clouds on a product manifold, our pipeline bridges the gap between discrete anatomical data and continuous geometric registration through three core iterative steps: (1) projecting these points into a continuous density proxy via a fast spherical Kernel Density Estimation (KDE); (2) applying ENCORE (Cole et al., 2025), a diffeomorphic warping framework, to estimate an incremental diffeomorphism that aligns the moving proxy toward the fixed target; and (3) applying the resulting warp directly to the point cloud of the moving subject. This design elegantly separates the domains: step (3) operates on the exact coordinates in the discrete space, whereas steps (1) and (2) compute the gradients in the continuous space. Figure 2 summarizes the pipeline.

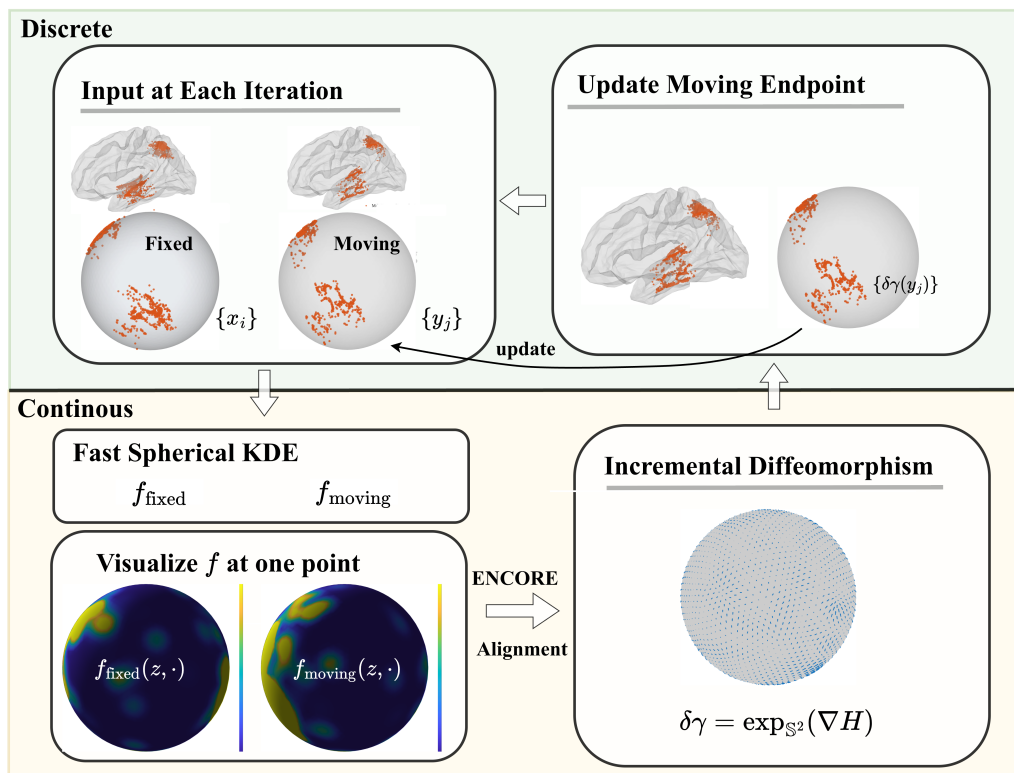


Figure 2. A diagram to illustrate our white matter endpoint-based alignment. For visualization, only the left hemisphere and the endpoints of the MdLF fiber bundle are shown. In the full analysis, both hemispheres and all streamline endpoints are used. A fast spherical KDE is used to compute the density proxies. Since the density proxy is defined on a two-dimensional space, we select a random point z and visualize $f(z, \cdot)$ on the sphere. The incremental diffeomorphism $\delta\gamma = \exp_{\mathbb{S}^2}(\nabla H)$, produced by the ENCORE engine (Cole et al., 2025) using the density proxy, is then applied directly to update the endpoints on the sphere. Throughout the pipeline, the endpoints of the fixed subject remain unchanged.

3.1. Objective and Problem Formulation

Let \mathcal{S}_1 and \mathcal{S}_2 be the left and right white-matter cortical surfaces of a subject, and let $\tilde{\Omega} = \mathcal{S}_1 \cup \mathcal{S}_2$. Both \mathcal{S}_1 and \mathcal{S}_2 are homeomorphic to the sphere \mathbb{S}^2 (Figure 1(B)(C)). Our primary objective is to establish accurate, point-to-point anatomical correspondence for $\tilde{\Omega}$ across different subjects by aligning the cortical endpoints of white-matter fiber bundles.

To capture white-matter fiber bundle-based structural connectivity, we rely on dMRI tractography, which computationally reconstructs long-range white-matter trajectories known as streamlines (Zhang et al., 2022). Because standard tractography often terminates prematurely in shallow white matter, we utilize the surface-enhanced tractography (SET) algorithm (St-Onge et al., 2018). SET enforces geometric constraints to ensure that reconstructed streamlines terminate exactly on the cortical boundary $\tilde{\Omega}$.

Given this framework, let $(\tilde{p}_1, \tilde{p}_2)$ denote a pair of endpoints belonging to a single streamline, where $\tilde{p}_1, \tilde{p}_2 \in \tilde{\Omega}$. Through standard parameterization, we map the folded cortical geometry to a spherical domain (Fischl et al., 1999). We denote (p_1, p_2) as the mapped image of $(\tilde{p}_1, \tilde{p}_2)$ on the product manifold $\Omega \times \Omega$, where $\Omega = \mathbb{S}_1^2 \cup \mathbb{S}_2^2$ represents the combined left and right spherical spaces. For subject i , the set of N_i streamline endpoints mapped onto the sphere is denoted as $\{(p_1^1, p_2^1), \dots, (p_1^{N_i}, p_2^{N_i})\}$.

These extracted point clouds serve as the input for alignment. However, establishing a direct discrete point-matching across subjects is mathematically intractable due to vastly different spatial patterns, varying point densities, and unequal streamline counts ($N_1 \neq N_2$). To overcome this, we elevate the discrete endpoints to a continuous domain, representing them via a smooth spatial density proxy. This continuous proxy acts as an iterative guiding signal: rather than treating it as a “true” statistical density to be perfectly estimated, our method leverages it to compute a mathematically rigorous diffeomorphic gradient, which is then applied directly back to align the discrete endpoint point cloud.

3.2. Continuous Intensity Proxies and Warping Energy

To construct the continuous density proxy, we map the spatial distribution of streamline endpoints into a smooth function through Kernel Density Estimation (KDE) (Wang et al., 2025). Specifically, given the endpoint pairs $\{(p_j^1, p_j^2)\}_{j=1}^N \subseteq \Omega \times \Omega$, we define the density proxy function $f : \Omega \times \Omega \mapsto [0, \infty]$ via a product kernel defined on $\Omega \times \Omega$:

$$f(x, y) = \frac{1}{N} \sum_{j=1}^N K_\sigma(x, p_j^1) K_\sigma(y, p_j^2), \quad (1)$$

where $K_\sigma(\cdot, \cdot)$ is the fast spherical heat kernel (Fischer et al., 1984; Camporesi, 1990; Nowak et al., 2019) evaluated on the spherical domain Ω , with $\sigma > 0$ being the bandwidth parameter. The exact formula of K_σ is given in Appendix B. The function defined in (1) is continuous and integrates to one over the product domain, i.e., $\int_\Omega \int_\Omega f(x, y) dx dy = 1$, so it defines a valid density on $\Omega \times \Omega$. To enforce symmetry, we define the symmetrized density $f_{\text{sym}}(x, y) = \frac{1}{2}(f(x, y) + f(y, x))$, and use f_{sym} as the continuous density proxy in practice. By construction, this guarantees that $f_{\text{sym}}(x, y) = f_{\text{sym}}(y, x)$.

Several techniques are used to make this KDE extremely fast. First, truncating the exponentially decaying high-frequency spectral terms in (A4) for K_σ reduces computational cost. Additionally, setting spatial contributions below a prescribed angular threshold to zero makes the resulting kernel matrix highly sparse. These optimizations make the KDE computationally efficient (Seguin et al., 2022). Moreover, because the spherical heat kernel admits a spectral representation (A4), its basis functions can be precomputed and reused across different bandwidths σ , reducing the kernel evaluation to a highly efficient matrix-vector contraction. Here, σ acts as a resolution parameter: smaller values preserve fine-scale endpoint structures, whereas larger values yield smoother representations that emphasize dominant fiber bundles (see Appendix B for details). The entire KDE computation can be reduced to efficient matrix-vector multiplication, avoiding the need for nested loops.

With each subject represented by a continuous function f , alignment reduces to finding a diffeomorphic reparameterization that brings a moving proxy f_2 into correspondence with a target proxy f_1 . While the squared \mathbb{L}^2 distance is a natural discrepancy measure, it is famously not invariant under diffeomorphic warping (i.e., $\|f_1 - f_2\| \neq \|f_1 \circ \gamma - f_2 \circ \gamma\|$) (Cole et al., 2025). This parameterization dependence can lead to spurious optimization minima driven by coordinate artifacts rather than anatomical differences.

To restore invariance, we apply the square-root (or Q -) mapping (Srivastava et al., 2010):

$$Q(f) = \sqrt{f}, \quad (2)$$

and define a modified group action of Γ_Ω (the set of all warping functions on Ω). For $q = Q(f)$ and $\gamma \in \Gamma_\Omega$,

$$(q * \gamma)(x, y) = q(\gamma(x), \gamma(y)) \sqrt{\det(D\gamma_x)} \sqrt{\det(D\gamma_y)}, \quad (3)$$

where, $q * \gamma$ represents the warped q function with a warping function γ , and $\det(D\gamma)$ denotes the Jacobian determinant. These Jacobian factors ensure that normalization is maintained under warping. Under this representation, the \mathbb{L}^2 distance becomes invariant (Cole et al., 2025), i.e., $\|q_1 - q_2\| = \|q_1 * \gamma - q_2 * \gamma\|$. Given a fixed target q_1 and a moving q_2 , we formulate the alignment energy as:

$$\inf_{\gamma \in \Gamma_\Omega} H(f_1, f_2 * \gamma), \quad \text{where} \quad H(f_1, f_2 * \gamma) = \iint_{\Omega^2} \left(q_1(x, y) - q_2(\gamma(x), \gamma(y)) \sqrt{\det(D\gamma_x) \det(D\gamma_y)} \right)^2 dx dy. \quad (4)$$

Note that this formulation inherently provides geometric regularization: extreme local deformations are naturally discouraged by the Jacobian determinants without requiring explicit regularization terms. For the domain $\Omega = \mathbb{S}_1^2 \cup \mathbb{S}_2^2$, refer to (A2) in the Appendix on how to define γ separately on each component.

Moreover, the formulation is inherently inverse-consistent, meaning that $H(f_1, f_2 * \gamma) = H(f_1 * \gamma^{-1}, f_2)$. Because Γ_Ω is a group, every mapping γ has an inverse γ^{-1} that also belongs to Γ_Ω . Therefore, taking the infimum over all $\gamma \in \Gamma_\Omega$ is equivalent to taking the infimum over all inverse mappings. As a result, the alignment energy in (4) is symmetric.

3.3. Iterative Alignment via Direct Endpoint Updates

While the objective in (4) provides a sound theoretical basis for alignment, standard implementations, e.g., ENCORE in Cole et al. (2025), optimize this function by repeatedly warping a discretized connectivity matrix. This grid-based approach introduces severe computational bottlenecks. Warping a grid representation requires evaluating Jacobian determinants at every vertex (i.e., the computation of warped q -function in (3)), typically via finite differences in tangent spaces. On coarse grids, these estimates are noisy and biased. As the warp is accumulated iteratively, these numerical errors compound, introducing artificial diffusion that steers the optimization away from the true minimizer. Refining the grid reduces bias but incurs a quadratic increase in computational cost due to the product domain $\Omega \times \Omega$.

Our core methodological contribution circumvents these limitations by eliminating the need to repeatedly warp a grid-based representation. By decoupling the gradient calculation from the spatial state update, we alternate between estimating a diffeomorphic warp increment from the continuous proxy and *directly updating the exact physical streamline endpoints*. The algorithm operates as follows:

1. **Continuous Gradient Estimation:** At iteration k , we freshly estimate the connectivity density $f_2^{(k)}$ directly from the current spatial locations of the warped point cloud using fast KDE introduced in Section 3.2. We then compute the gradient of the energy functional ∇H based on a truncated basis expansion (detailed in Appendix A and Cole et al. (2025)).
2. **Discrete Endpoint Update:** We generate a small incremental diffeomorphic warp $\delta\gamma$ via the exponential map of the gradient. Crucially, instead of applying this warp to the Q function of density $f_2^{(k)}$ with a Jacobian correction (i.e., Equation (3)), *we apply $\delta\gamma$ exclusively to the discrete coordinates of the moving streamline endpoints*.

By utilizing the continuous density merely as a gradient-generating mechanism, we apply all spatial updates directly to the discrete endpoints, entirely avoiding grid-based interpolation errors. Furthermore, because spatial smoothing and diffeomorphic warping are non-commutative operations

($\text{Smooth}(f * \gamma) \neq \text{Smooth}(f) * \gamma$), iteratively warping a pre-smoothed density grid introduces progressive numerical blurring that degrades the anatomical signal. Warping the exact physical endpoints and re-estimating the density from scratch at each step prevents this systematic drift. By preserving the precise spatial localization of the data throughout the optimization, this direct point-cloud alignment is able to achieve a significantly more accurate correspondence of the structural connectivity patterns generated by white-matter streamlines.

The aggregated numerical procedure is detailed in Algorithm 1. At each iteration, we compute a smooth tangent vector field on the base manifold \mathbb{S}^2 . The incremental spatial warp is then obtained by applying the Riemannian exponential map of the sphere point-wise to evaluate the displacement along this vector field. In the context of optimization on the space of diffeomorphisms, this point-wise application acts as a retraction. While the exact theoretical flow of a smooth vector field is unconditionally diffeomorphic, this point-wise retraction guarantees a diffeomorphism only for sufficiently small step sizes, which ensures that adjacent geodesic trajectories do not cross. By enforcing a small step size in our gradient descent scheme and terminating after a finite number of iterations, the composition of these incremental updates ensures that the overall output transformation remains diffeomorphic.

Algorithm 1 Direct Point-Cloud Cortical Alignment on $\Omega = \mathbb{S}_1^2 \cup \mathbb{S}_2^2$

- 1: **Input:** Target endpoints $\{x_i\}$ and Source endpoints $\{y_j^{(0)}\}$
- 2: Initialize $k = 0$, cumulative warps $\gamma^{1(0)} = \gamma^{2(0)} = \gamma_{\text{id}}$, step size δ , tolerance ϵ
- 3: Compute target connectivity f_1 from $\{x_i\}$ via spherical heat kernel (1); obtain Q -transform $q_1 = Q(f_1)$
- 4: **loop**
- 5: Compute moving connectivity $f_2^{(k)}$ from current endpoints $\{y_j^{(k)}\}$ via heat kernel (1)
- 6: Obtain Q -transform $q_2^{(k)} = Q(f_2^{(k)})$
- 7: Compute the gradients ∇H_{γ^1} and ∇H_{γ^2} using q_1 and $q_2^{(k)}$ according to (A3)
- 8: **if** $\|\nabla H_{\gamma^1}\|_{\mathbb{L}^2} < \epsilon$ **and** $\|\nabla H_{\gamma^2}\|_{\mathbb{L}^2} < \epsilon$ **then**
- 9: **break**
- 10: **end if**
- 11: Compute small incremental warps: $\delta\gamma^1 \leftarrow \exp_{\mathbb{S}^2}(\delta\nabla H_{\gamma^1})$, $\delta\gamma^2 \leftarrow \exp_{\mathbb{S}^2}(\delta\nabla H_{\gamma^2})$
- 12: Form joint incremental warp $\delta\gamma = (\delta\gamma^1, \delta\gamma^2)$
- 13: **Direct Endpoint Update:** $\{y_j^{(k+1)}\} \leftarrow \{\delta\gamma(y_j^{(k)})\}$
- 14: Update cumulative tracking (optional): $\gamma^{(k+1)} \leftarrow \gamma^{(k)} \circ \delta\gamma$
- 15: $k \leftarrow k + 1$
- 16: **end loop**
- 17: **Output:** Aligned Endpoints $\{y_j^{(k)}\}$, Final Diffeomorphism $\gamma^{(k)}$

Note: \exp denotes the point-wise Riemannian exponential map on the base manifold \mathbb{S}^2 , which acts as a retraction for sufficiently small step sizes δ .

4. Evaluation and Implementation Details

4.1. Endpoints Alignment Evaluation Method

Evaluating the accuracy of cortical surface alignment is inherently challenging due to the absence of a ground-truth diffeomorphic mapping between subjects. Furthermore, while whole-brain white matter tractography broadly captures the brain's structural wiring, it inevitably produces a mixture of true, well-documented anatomical fiber bundles and erroneous or spurious streamlines (Maier-Hein et al., 2017). To increase the accuracy and biological validity of our alignment measurement, we evaluate performance by relying exclusively on well-characterized, major fiber tracts. If two subjects are accurately aligned at the SC connectivity level, their corresponding major bundles should occupy highly overlapping regions on the cortical surface.

To isolate these structures, we employ RecoBundlesX, a multi-atlas white matter bundle segmentation framework, to extract major fiber bundles from individual subjects. RecoBundlesX is an enhanced version of the RecoBundles algorithm (Garyfallidis et al., 2018), incorporating multi-parameter fusion to improve bundle segmentation accuracy and robustness. This approach allows for precise and reliable extraction of white matter pathways across subjects. The segmentation procedures were implemented using the Scilpy (St-Onge et al., 2023) pipeline.

To quantify this anatomical agreement, we define the **Connectivity-level Overlap Coefficient**, which directly measures the overlap of suprathreshold connectivity patterns for these specific bundles after registration. Unlike a pointwise distance metric, the overlap coefficient compares whether the same major connections are structurally present in both subjects after alignment, making it well suited for evaluating whether fiber-tract endpoints have been brought into correspondence. Specifically, we partition the sphere into a discrete triangular mesh $\Delta = \{\Delta_1, \dots, \Delta_K\}$ (using an icosphere grid with $G = 4, V = 2562, K = 5120$; see Section 4.2 for details). Let $C_{a,b}^i$ denote the number of streamlines in subject $i \in \{1, 2\}$ whose endpoints fall into the triangle pair Δ_a and Δ_b . With n_i denoting the total number of streamlines belonging to the specific tract of interest in the subject i , we define the overlap coefficient at the threshold $\tau \geq 0$ as:

$$\text{Overlap Coefficient}(\tau) = \frac{\sum_{a \leq b} \mathbf{1}\left(\frac{C_{a,b}^1}{n_1} > \tau\right) \mathbf{1}\left(\frac{C_{a,b}^2}{n_2} > \tau\right)}{\min\left(\sum_{a \leq b} \mathbf{1}\left(\frac{C_{a,b}^1}{n_1} > \tau\right), \sum_{a \leq b} \mathbf{1}\left(\frac{C_{a,b}^2}{n_2} > \tau\right)\right)}. \quad (5)$$

This score ranges from 0 to 1. A higher value indicates that the two subjects share more of the same major connections above the threshold. In this way, the connectivity-level overlap coefficient rigorously evaluates whether registration preserves and aligns the endpoints of anatomically meaningful fiber tracts.

Because the estimation of the continuous gradients relies on the diffusion parameter σ in (1), the choice of σ directly influences the final diffeomorphism produced by Algorithm 1. It is therefore important to select an appropriate value. Since our objective is to maximize anatomical correspondence, we choose σ based on the connectivity-level overlap coefficient, selecting the value that yields the highest overlap for major fiber tract alignment. We detail the empirical selection of σ for real data in Section 6.2.

4.2. Discretization

Although the continuous intensity proxy function is theoretically defined on every point in $\Omega \times \Omega$, in practice it is evaluated on a discrete set of vertex pairs $\{(x_i, x_j)\}$, where each $(x_i, x_j) \in \Omega \times \Omega$ and the vertices lie on a spherical grid. We adopt an icosphere discretization, obtained by recursively subdividing the faces of an icosahedron and projecting the newly created vertices onto the sphere. The icosphere yields near-uniform triangle areas, which aligns with the discretization assumption of approximately uniform sampling. Moreover, the subdivision process is hierarchical: vertices at lower resolutions form a subset of those at higher resolutions. This property makes it straightforward to switch between resolutions. The number of vertices V in an icosphere grid follows $V = 10 * 4^G + 2$, where G denotes the number of subdivision levels. In this paper, unless otherwise specified, we set $G = 4$, which corresponds to $V = 2562$ vertices. Using a finer grid (e.g., an icosphere with $G = 5$) improves the accuracy of the gradient estimation step, but significantly increases the computational cost.

5. Simulation Study with Ground-Truth

To evaluate our endpoint-based method in a controlled setting, we simulate point-cloud data from a known underlying connectivity density function and apply synthetic ground-truth warpings. We demonstrate that the proposed approach accurately recovers the underlying diffeomorphic trans-

formation, even in challenging scenarios where the true deformation is large and the grid resolution is relatively coarse.

We begin by specifying the ground-truth density function used throughout the accuracy and robustness simulations. Let

$$h_\kappa(t) := e^{\kappa t}, \quad t \in [-1, 1]. \quad (6)$$

Using a von Mises–Fisher (vMF) kernel, we define the joint probability density $f(x, y)$ of the streamline endpoints on the product manifold $\Omega \times \Omega$ as:

$$f(x, y) = \begin{cases} \alpha \cdot \frac{h_\kappa(x \cdot y)}{2(4\pi)^2(\sinh \kappa/\kappa)} & \text{if } x, y \in \mathbb{S}_1^2 \text{ or } x, y \in \mathbb{S}_2^2, \\ (1 - \alpha) \cdot \frac{1}{2(4\pi)^2} & \text{if } (x, y) \in \mathbb{S}_1^2 \times \mathbb{S}_2^2 \text{ or } \mathbb{S}_2^2 \times \mathbb{S}_1^2. \end{cases} \quad (7)$$

This formulation is designed to capture key topological features of true neural wiring. Empirical brain connectivity data typically exhibit stronger and denser within-hemisphere connections than cross-hemisphere connections. To reflect this property, we set the mixture weight $\alpha = 0.85$, thereby assigning significantly greater probability mass to intra-hemispheric interactions.

Crucially, the parameter $\kappa > 0$ controls the concentration of the vMF kernel, which governs the spatial dispersion of the simulated fiber bundles. In a biological context, κ dictates how tightly clustered the simulated endpoints are: a higher κ produces sharply localized density peaks (mimicking dense, highly structured major white-matter tracts), whereas a lower κ generates more diffuse, unstructured connection patterns. Throughout the simulations, we fix $\kappa = 10$, which provides a realistic balance representing moderately clustered structural connectivity.

5.1. Alignment Accuracy Evaluation

To evaluate the accuracy of the proposed endpoint-based method under large deformations, we consider a simple spherical example. In this setting, we demonstrate that the endpoint-based approach improves estimation accuracy compared to ENCORE (Cole et al., 2025) when the ground-truth diffeomorphism induces substantial distortion. Specifically, we use the ground-truth density function f defined in (7) and sample a fixed number of streamlines from this distribution. Given a known ground-truth diffeomorphism γ_{truth} that produces large deformation (see the left panel of Figure 3), we independently draw the same number of streamlines from f and transform their endpoints using γ_{truth} . Note that increasing the number of sampled streamlines improves estimation accuracy, as the empirical distribution more closely approximates the true density f . To reflect the real-data setting described in Section 6.1, we use 1×10^6 streamlines in this experiment.

We then apply both ENCORE and our endpoint-based method to estimate the deformation. For a fair comparison, both methods use the same stopping criterion ϵ . For the kernel diffusion bandwidth parameter σ , we set $\sigma = 0.005$ for the endpoint based method (see Section 6.2). For ENCORE, we evaluate multiple kernel scales and report the best result based on mean squared error relative to the ground truth. A visualization is provided in Figure 3.

The middle column of Figure 3 shows the estimated warpings using ENCORE and our endpoint-based method. The right panel shows the tangent vector fields $\log_{\gamma_{\text{ENCORE}}}(\gamma_{\text{truth}})$ and $\log_{\gamma_{\text{endpoint}}}(\gamma_{\text{truth}})$, which represent the displacements from the ENCORE estimate γ_{ENCORE} to the true warping, and from the endpoint-based estimate γ_{endpoint} to the true warping.

Our endpoint-based method achieves higher accuracy than ENCORE. Specifically, ENCORE attains a mean squared error of 0.0359, whereas our method achieves a lower error of 0.0258. For small angles on the unit sphere, mean squared error is approximately equivalent to mean angular distance, making this comparison geometrically meaningful. Under large deformations, ENCORE struggles to accurately estimate the Jacobian determinant, which limits its ability to recover the true transformation.

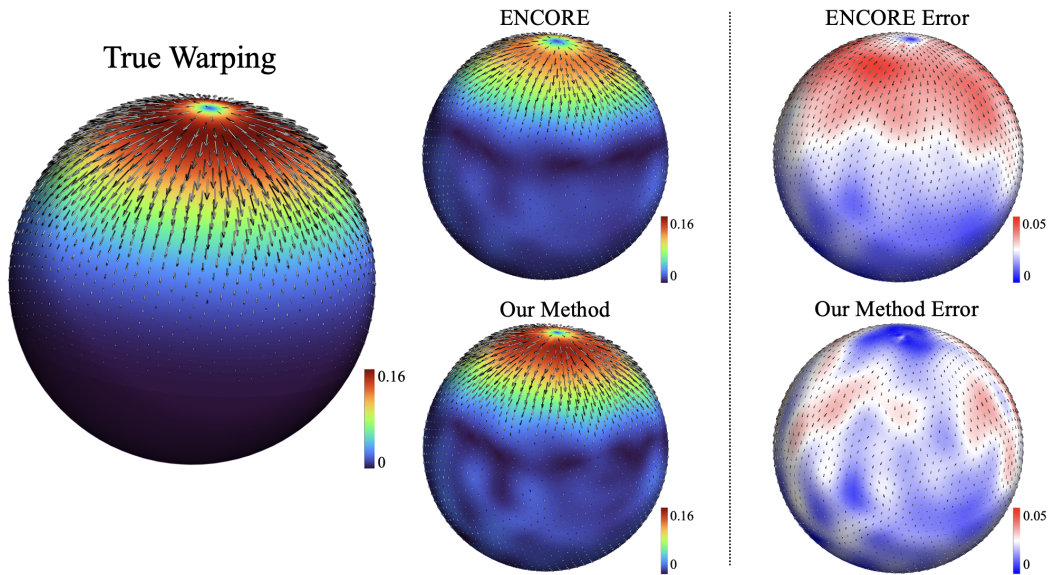


Figure 3. Left: The left panel displays the ground-truth warping together with the warpings estimated by the ENCORE algorithm and the endpoint-based algorithm (Algorithm 1). The background color represents the magnitude of each warping, as indicated by the colorbar. **Right:** The error of the ENCORE estimate relative to the ground truth is defined as $\log_{\gamma_{\text{ENCORE}}}(\gamma_{\text{truth}})$, the tangent vector at the ENCORE-estimated warping that points toward the ground-truth warping on the sphere. Similarly, the error of the endpoint-based estimate is defined as $\log_{\gamma_{\text{endpoint}}}(\gamma_{\text{truth}})$, the tangent vector at the endpoint-estimated warping that points toward the ground-truth warping. The background color represents the magnitudes of these displacement vectors, as indicated by the colorbar.

5.2. Robustness to Grid Resolution

As discussed earlier, the ENCORE algorithm relies on estimating the determinant of the Jacobian matrix, whereas our endpoint-based method avoids this step. Consequently, changes in the underlying grid used for connectivity estimation have a greater impact on ENCORE than on the endpoint-based method.

To assess robustness to grid resolution, we apply both ENCORE and the endpoint-based method on icosphere discretizations with subdivision levels $G = 4$ ($V = 2562$) and $G = 5$ ($V = 10242$). The ground-truth connectivity function f is defined in (7). The corresponding warping function γ is shown in Appendix D, Figure A2. Although the ground-truth warping is defined over the entire sphere, the figure displays its icosphere-4 discretization for illustration. The selected ground-truth warping exhibits heterogeneous deformation across the domain, with variations in both magnitude and direction, thereby rendering the estimation of the underlying diffeomorphism a nontrivial task. We evaluate alignment accuracy by measuring the discrepancy between the estimated and true warping using mean angular distance and mean L_2 distance. In each experiment, we first independently sample 1×10^6 streamlines for both the fixed and moving subjects according to the ground-truth connectivity f . For the fixed subject, the sampled streamline endpoints are then transformed using the prescribed ground-truth warping γ . Alignment is then performed to register the moving subject to the fixed subject using both ENCORE and the **endpoint-based** method (Algorithm 1). All experiments are conducted on icosphere meshes with 2,562 vertices (level 4) and 10,242 vertices (level 5), using the same stopping criterion for both methods. For the endpoint-based method, we set the kernel diffusion parameter to $\sigma = 0.005$, as discussed in Section 6.2. For ENCORE, we evaluate multiple kernel scales and report the best-performing result based on the mean angular distance to the ground truth.

To focus on regions with substantial deformation, we restrict evaluation to vertices whose ground-truth warping magnitude is at least the median across all vertices (i.e., the top 50% by magnitude). On these vertices, we report: (1) the mean angular distance between the true and estimated warping vectors, and (2) the mean L_2 distance between the true warped vertices and the estimated warped

vertex positions. The results are shown in Table 1. Compared with ENCORE, our endpoint-based method is more robust to the change from icosphere 4 to icosphere 5, and it produces estimates that are closer to the ground truth.

Table 1. Warping estimation performance (evaluation restricted to vertices whose ground-truth warping magnitude \geq median).

Method	Icosphere (vertices)	Mean angular ($^\circ$)	Mean L_2
ENCORE	Icosphere 4 (2,562)	15.95 $^\circ$	0.0544
Endpoints	Icosphere 4 (2,562)	10.06 $^\circ$	0.0367
ENCORE	Icosphere 5 (10,242)	13.01 $^\circ$	0.0483
Endpoints	Icosphere 5 (10,242)	9.93 $^\circ$	0.0362

6. Real Data Analysis

6.1. Dataset and Preprocessing

We evaluate the proposed endpoint-based alignment method using data from the Human Connectome Project (HCP) a large-scale neuroimaging study designed to characterize human brain connectivity in a cohort of healthy adults. The HCP provides multimodal MRI acquisitions, including structural MRI, diffusion MRI (dMRI), and both resting-state and task-based functional MRI, enabling detailed reconstruction of anatomical and functional brain networks.

The dMRI data are processed using the structural connectivity analysis SBCI pipeline (Cole et al., 2021). This pipeline reconstructs cortical surfaces and computes their spherical parameterizations via FreeSurfer (Fischl et al., 1999). White matter fiber tracts connecting the cortical surfaces are then estimated using SET (St-Onge et al., 2018), yielding streamline-based representations of structural connectivity. For each subject, approximately 5×10^5 to 10^6 streamlines are generated. In all subsequent analyses, we retain only the corresponding streamline endpoints.

To assess alignment accuracy, we evaluate whether endpoints associated with major white matter fiber bundles exhibit improved cross-subject agreement after registration. Specifically, we quantify the overlap of bundle-specific endpoint distributions across subjects and compare the proposed endpoint-based method with commonly used registration approaches. The underlying hypothesis is that improved anatomical alignment of connectomes should yield higher inter-subject agreement in endpoint locations, as measured by a connectivity-level overlap coefficient.

6.2. Hyperparameter Selection based on Real Data

Recall that the bandwidth parameter σ in (1) controls the smoothness of the KDE estimated from the endpoints. Smaller values of σ preserve the discrete structure of the endpoints, yielding sharp, localized peaks, whereas larger values produce smoother estimates. Since our goal is to align endpoints corresponding to major fiber tracts, we select σ based on alignment performance on the fiber bundles of interest.

As discussed in Section 4.1, we select the bandwidth parameter σ in (1) using the connectivity-level overlap coefficient defined in (5). Specifically, we split the dataset into training and testing sets and run Algorithm 1 on the training subjects over a range of diffusion times σ , obtaining warped results for each value. For each case, we compute the connectivity-level overlap coefficient between the template and the warped training subjects' streamlines, evaluated across multiple regions of interest. The results are summarized in Figure 4. Overall, $\sigma = 0.005$ yields the highest weighted overlap coefficient, whether using equal weights across major fiber tracts or weights proportional to the mean number of endpoints in the tracts of interest, compared to other choices. In the subsequent analysis, we use $\sigma = 0.005$, and all analyses are conducted on the test subjects.

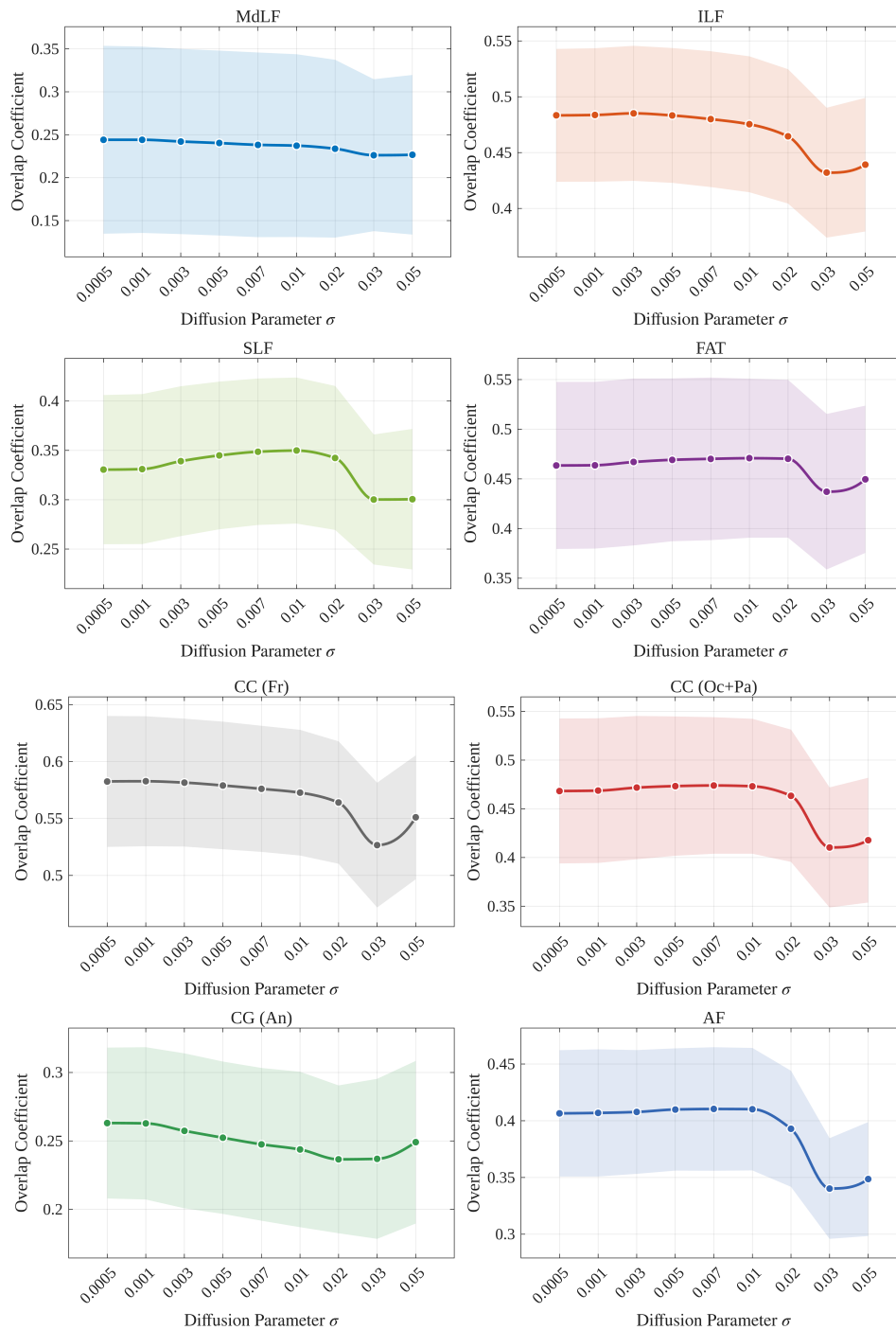


Figure 4. Optimization of the spherical heat kernel bandwidth. The connectivity-level overlap coefficient was computed between the template and 50 aligned moving subjects using varying diffusion parameters (σ). The overall performance demonstrates that $\sigma = 0.005$ optimally resolves the spatial density required for successful endpoint alignment.

6.3. Alignment Evaluation on Real Data

We evaluate alignment accuracy using the connectivity-level overlap coefficient defined in (5). Using the test subjects, we compare our **endpoint-based** method (Algorithm 1) with raw unaligned streamline endpoint data (**Native**), **MSMail** (Robinson et al., 2014) and **ENCORE** (Cole et al., 2025). The connectivity-level overlap coefficient results for eight major fiber bundle tracts are shown in Figure 5. Our endpoint-based method achieves higher overlap coefficients across most major fiber tracts, indicating improved connectivity-based alignment. Note that the overlap coefficient after alignment is also influenced by the number of streamlines within each tract of interest, as well as the

distribution of their original endpoints. The MMD coefficient result is provided in Appendix C. As the connectivity-level overlap coefficient evaluates connectivity-level alignment, the MMD coefficient provides an additional validation of the distribution-level discrepancy between streamline endpoint distributions. Here, we use only the streamline endpoints from the left hemisphere. The MMD coefficient is nonnegative, with larger values indicating greater discrepancy between distributions.

In the connectivity-level overlap coefficient evaluation reported in Figure 5, we consider the following major fiber bundles: Occipital and Parietal fibers of the Corpus Callosum (CC (Oc+Pa)), Superior Longitudinal Fasciculus (SLF), Frontal fibers of the Corpus Callosum (CC (Fr)), Arcuate Fasciculus (AF), Middle Longitudinal Fasciculus (MdLF), Frontal Aslant Tract (FAT), anterior portion of the Cingulum Bundle (CG (An)), and Inferior Longitudinal Fasciculus (ILF). The commissural fibers, CC (Oc+Pa) and CC (Fr), connect the two hemispheres, whereas the association fibers, SLF, AF, MdLF, FAT, CG (An), and ILF, connect regions within the same hemisphere. Among the within-hemisphere bundles, AF, SLF, MdLF, and FAT are long-range language-related tracts; CG (An) is a limbic-related tract; and ILF is associated with the visual pathway. ENCORE achieves larger overlap coefficients than both the native and MSMAll methods. Compared with ENCORE, our proposed endpoint-based method achieves larger overlap coefficients for all fiber bundles except CG (An). Moreover, from the MMD results in the supplementary Figure A1, we see that our method achieves better results for all fiber bundles on average than ENCORE, native and MSMAll.

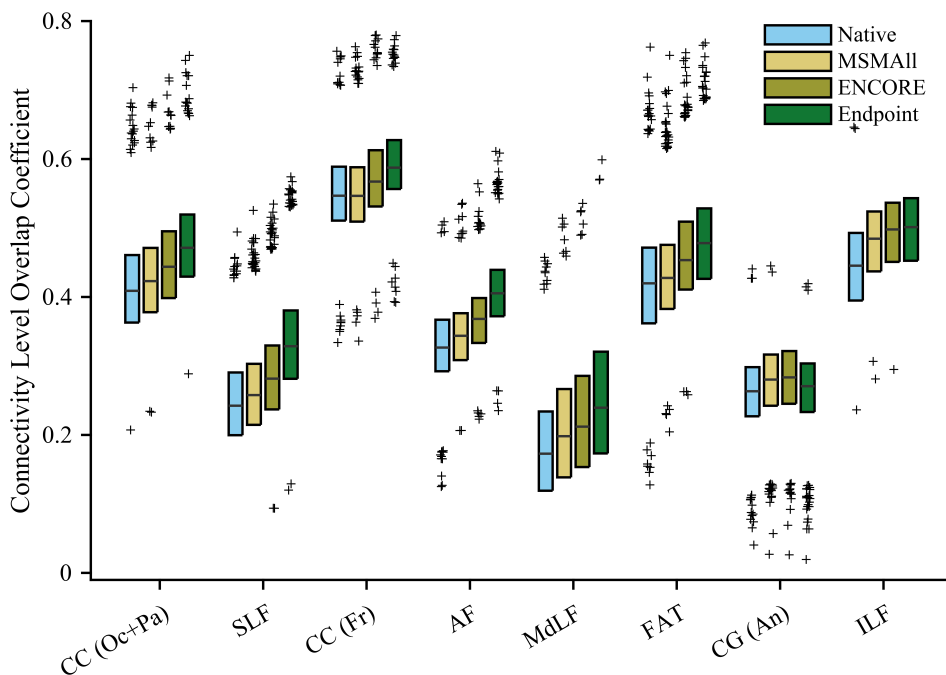


Figure 5. Connectivity-level overlap coefficient for eight major fiber bundles.

6.4. Computational Complexity Analysis and GPU Acceleration

Although the algorithm that operates directly on the endpoints achieves higher accuracy than previous methods, repeatedly warping the endpoints and estimating connectivity at each iteration is computationally expensive. In this section, we explore strategies to accelerate the process.

From the robustness analysis in Section 5.2, our endpoint-based method does not require high-resolution data to achieve accurate alignment. Consequently, the computational cost can be kept at a relatively efficient level. Moreover, when estimating f from endpoints using the spherical heat kernel, a strict spatial cutoff is imposed, resulting in a sparse kernel matrix that reduces computational cost, as discussed in Appendix B.

To assess potential acceleration, we summarize the runtime breakdown of each implementation step in Table 2. Both the gradient estimation step and the KDE evaluation step become substantially

more expensive as the resolution increases. With GPU acceleration, both steps are significantly faster. However, the KDE evaluation step continues to dominate the overall runtime and remains the primary computational bottleneck. We note that the KDE evaluation step scales quadratically with the number of grid vertices, i.e., $O(V^2)$.

The total number of iterations required for convergence depends on the bandwidth parameter σ , step size δ , and stopping criterion ϵ . For $\sigma = 0.005$, $\delta = 0.1$, and $\epsilon = 10^{-6}$, the algorithm converges in approximately 60 iterations on the icosphere 4 grid and approximately 450 iterations on the icosphere 5 grid.

Table 2. Runtime breakdown (%) for different icosphere resolutions and execution settings. Percentages are relative to the total runtime and may not sum to exactly 100% due to rounding. Values in parentheses indicate the average runtime per iteration.

Setting	Resolution	Gradient Estimation	Endpoint Update (Warp)	KDE Evaluation
CPU	icosphere 4	26.98% (0.9014s)	19.79% (0.6612s)	56.62% (1.7790s)
CPU	icosphere 5	29.74% (12.9725s)	1.33% (0.5817s)	68.92% (30.0631s)
GPU	icosphere 4	0.51% (0.0093s)	40.73% (0.7402s)	58.76% (1.0677s)
GPU	icosphere 5	1.23% (0.1365s)	7.66% (0.8501s)	91.11% (10.1121s)

7. Conclusions and Discussion

The proposed approach leverages streamline endpoint information to align cortical surfaces across subjects, yielding improved alignment accuracy as quantified by the connectivity-level overlap coefficient on major fiber bundles. Streamline endpoints derived from white matter tracts encode connectivity patterns that can be directly incorporated into the alignment objective. Optimization of this objective produces a spherical deformation that is guaranteed to be diffeomorphic.

In contrast to methods that attempt to estimate a true underlying continuous connectivity function, the present approach operates directly on endpoint representations, thereby avoiding this additional source of approximation error. Endpoint information is incorporated at each iteration, eliminating the need for explicit Jacobian estimation and reducing numerical inaccuracies. Furthermore, the computational accuracy of the method exhibits weak dependence on the choice of spherical grid resolution. This robustness allows accurate alignment to be achieved even on relatively coarse discretizations, leading to reduced computational cost without sacrificing performance.

This algorithm provides a geometrically rigorous framework for generating diffeomorphic deformations based on the Fisher–Rao metric, and achieves strong connectivity-level and endpoint distribution-level alignment performance on major fiber tracts. The primary limitation is the computational cost of the spherical KDE evaluation step, which remains the main computational bottleneck. In the literature, numerous neural network-based alignment methods (Balakrishnan et al., 2019; Zhao et al., 2021) achieve greater computational efficiency than the gradient-based endpoint approach proposed in this paper. However, such methods typically depend on explicit additional regularization terms to enforce smoothness and invertibility of the deformation. Our method provides a theoretically grounded and geometrically principled foundation that could be integrated with deep learning approaches to improve computational efficiency while preserving high alignment accuracy and interpretability.

Beyond the empirical evaluation presented in this work, several additional aspects of the algorithm merit further discussion, particularly computational efficiency, the role of endpoint selection in the optimization procedure, and the choice of the bandwidth parameter σ . In the following, we discuss these considerations and outline several directions for future improvement.

If the goal is to align only specific fiber tracts rather than all streamlines on the cortical surface, one could restrict the procedure to the endpoints of the tracts of interest. In this case, kernel density estimation is performed using only these endpoints, the corresponding gradient is computed, and

the resulting deformation is applied exclusively to them. This approach yields a substantially higher connectivity-level overlap coefficient for the selected tracts compared to using all streamlines. However, we choose to use all streamlines on the cortical surface because endpoints outside the tracts of interest provide important regularization in the optimization. Without these additional constraints, the resulting diffeomorphism may become unstable, producing large and unrealistic deformations in unconstrained regions in order to better align only the selected endpoints.

In Section 6.2, we select the diffusion bandwidth parameter σ using the overlap coefficients of major fiber tracts. In addition, we also performed a leave-one-out log-likelihood cross-validation (LCV) procedure based on the kernel matrices. Specifically, for each candidate σ , we construct a kernel-smoothed density estimate and evaluate its predictive performance using leave-one-out likelihood. For each fiber endpoint pair (p_j^1, p_j^2) , the contribution of the j -th fiber is removed from the density estimate, and the resulting model is used to predict the connectivity at that fiber's barycentric endpoints. The LCV score is defined as

$$\text{LCV}(\sigma) = \frac{1}{N} \sum_{j=1}^N \log \hat{f}_\sigma^{(-j)}(p_j^1, p_j^2), \quad (8)$$

where $\hat{f}_\sigma^{(-j)}$ denotes the leave-one-out density estimate obtained with the j -th fiber excluded. The optimal bandwidth is selected as the value of σ that maximizes this score. This cross-validation procedure is computationally efficient within the KDE framework adopted in this paper (Appendix B). The optimal bandwidth selected by this procedure was also $\sigma = 0.005$.

In Section 6.4, the runtime breakdown indicates that KDE evaluation is the primary computational bottleneck of our algorithm. To reduce this cost, the KDE can be evaluated once every k iterations rather than at every iteration. Specifically, the endpoints are updated (Endpoint Update) and the continuous density proxy is recomputed (KDE Evaluation) only every k steps. During the intermediate iterations, ENCORE is used to directly warp the current density proxy without recomputing the KDE. This strategy reduces the overall computational cost while preserving the update dynamics of the algorithm.

Our algorithm also supports a multiresolution strategy. Specifically, we first run Algorithm 1 on a coarser grid (e.g., icosphere 3 with 642 vertices) and apply the resulting warping to the streamline endpoints. We then rerun Algorithm 1 on these updated endpoints using a finer grid (e.g., icosphere 4 with 2562 vertices), and compose the resulting warping with the previous one to obtain the final transformation. In this multiscale framework, the bandwidth parameter σ can also vary across resolutions; for example, a larger σ can be used on the coarse grid and gradually reduced on finer grids. This approach accelerates convergence when the goal is to obtain a warping on a very fine grid, since computations on the coarser grid are significantly less expensive. The algorithm captures large deformations on a coarser grid and then refines them on a finer grid. However, the performance of this multiresolution strategy may depend on the choice of grid hierarchy, refinement levels, and stopping criteria. Poor choices of resolution hierarchy or stopping criteria may lead to suboptimal alignment performance.

Author Contributions: Y.X.: Conceptualization, Methodology, Validation, Formal analysis, Investigation, Data curation, Writing—original draft preparation, Visualization; M.C.: Conceptualization, Methodology, Software, Data curation; Z.Z.: Conceptualization, Methodology, Resources, Writing—review and editing, Supervision, Project administration. All authors have read and agreed to the published version of the manuscript.

Funding: This research received no external funding.

Institutional Review Board Statement: Not applicable.

Informed Consent Statement: Not applicable.

Data Availability Statement: The data used in this study were obtained from the Human Connectome Project (HCP) database and are publicly available at <https://www.humanconnectome.org/study/hcp-young-adult>.

Access to the data requires registration and acceptance of the HCP Open Access Data Use Terms. The source code used in this study is available at: <https://github.com/MartyCole/Encore/>.

Conflicts of Interest: The authors declare no conflict of interest.

References

- Balakrishnan, G., Zhao, A., Sabuncu, M. R., Guttag, J., and Dalca, A. V. (2019). Voxelmorph: a learning framework for deformable medical image registration. *IEEE transactions on medical imaging*, 38(8):1788–1800.
- Camporesi, R. (1990). Harmonic analysis and propagators on homogeneous spaces. *Physics Reports*, 196(1-2):1–134.
- Cheng, J., Dalca, A. V., Fischl, B., Zöllei, L., Initiative, A. D. N., et al. (2020). Cortical surface registration using unsupervised learning. *NeuroImage*, 221:117161.
- Cole, M., Murray, K., St-Onge, E., Risk, B., Zhong, J., Schifitto, G., Descoteaux, M., and Zhang, Z. (2021). Surface-based connectivity integration: An atlas-free approach to jointly study functional and structural connectivity. *Human Brain Mapping*, 42(11):3481–3499.
- Cole, M., Xiang, Y., Consagra, W., Srivastava, A., Qiu, X., and Zhang, Z. (2025). Alignment of continuous brain connectivity. *arXiv preprint arXiv:2503.15830*.
- Das, S. R., Avants, B. B., Grossman, M., and Gee, J. C. (2009). Registration-based cortical thickness measurement. *Neuroimage*, 45(3):867–879.
- Fischer, H. R., Jungster, J. J., and Williams, F. L. (1984). The heat kernel on the two-sphere. *Adv. Math*, 54(2):226–232.
- Fischl, B., Sereno, M. I., and Dale, A. M. (1999). Cortical surface-based analysis: Ii: inflation, flattening, and a surface-based coordinate system. *Neuroimage*, 9(2):195–207.
- Garyfallidis, E., Côté, M.-A., Rheault, F., Sidhu, J., Hau, J., Petit, L., Fortin, D., Cunanne, S., and Descoteaux, M. (2018). Recognition of white matter bundles using local and global streamline-based registration and clustering. *NeuroImage*, 170:283–295.
- Glasser, M. F., Coalson, T. S., Robinson, E. C., Hacker, C. D., Harwell, J., Yacoub, E., Ugurbil, K., Andersson, J., Beckmann, C. F., Jenkinson, M., et al. (2016). A multi-modal parcellation of human cerebral cortex. *Nature*, 536(7615):171–178.
- Gutman, B., Leonardo, C., Jahanshad, N., Hibar, D., Eschenburg, K., Nir, T., Villalon, J., and Thompson, P. (2014). Registering cortical surfaces based on whole-brain structural connectivity and continuous connectivity analysis. In *International Conference on Medical Image Computing and Computer-Assisted Intervention*, pages 161–168. Springer.
- Jbabdi, S., Sotiropoulos, S. N., Haber, S. N., Van Essen, D. C., and Behrens, T. E. (2015). Measuring macroscopic brain connections in vivo. *Nature neuroscience*, 18(11):1546–1555.
- Lazar, M. (2010). Mapping brain anatomical connectivity using white matter tractography. *NMR in Biomedicine*, 23(7):821–835.
- Li, J., Tuckute, G., Fedorenko, E., Edlow, B. L., Dalca, A. V., and Fischl, B. (2024). Josa: Joint surface-based registration and atlas construction of brain geometry and function. *Medical image analysis*, 98:103292.
- Maier-Hein, K. H., Neher, P. F., Houde, J.-C., Côté, M.-A., Garyfallidis, E., Zhong, J., Chamberland, M., Yeh, F.-C., Lin, Y.-C., Ji, Q., et al. (2017). The challenge of mapping the human connectome based on diffusion tractography. *Nature Communications*, 8(1):1349.
- Milano, M., Guzzi, P. H., Tymofieva, O., Xu, D., Hess, C., Veltri, P., and Cannataro, M. (2017). An extensive assessment of network alignment algorithms for comparison of brain connectomes. *BMC bioinformatics*, 18(Suppl 6):235.
- Nowak, A., Sjögren, P., and Szarek, T. Z. (2019). Sharp estimates of the spherical heat kernel. *Journal de Mathématiques Pures et Appliquées*, 129:23–33.
- Osmanlıoğlu, Y., Alappatt, J. A., Parker, D., and Verma, R. (2020). Connectomic consistency: a systematic stability analysis of structural and functional connectivity. *Journal of neural engineering*, 17(4):045004.
- Robinson, E. C., Jbabdi, S., Glasser, M. F., Andersson, J., Burgess, G. C., Harms, M. P., Smith, S. M., Van Essen, D. C., and Jenkinson, M. (2014). Msm: a new flexible framework for multimodal surface matching. *Neuroimage*, 100:414–426.
- Seguin, C., Smith, R. E., Zalesky, A., et al. (2022). Connectome spatial smoothing (css): Concepts, methods, and evaluation. *NeuroImage*, 250:118930.

- Srivastava, A., Klassen, E., Joshi, S. H., and Jermyn, I. H. (2010). Shape analysis of elastic curves in euclidean spaces. *IEEE Transactions on Pattern Analysis and Machine Intelligence*, 33(7):1415–1428.
- St-Onge, E., Daducci, A., Girard, G., and Descoteaux, M. (2018). Surface-enhanced tractography (set). *NeuroImage*, 169:524–539.
- St-Onge, E., Schilling, K. G., and Rheault, F. (2023). Bundleseg: A versatile, reliable and reproducible approach to white matter bundle segmentation. In *International Workshop on Computational Diffusion MRI*, pages 47–57. Springer.
- Wang, L., Li, D., and Zhang, Z. (2025). Riemannian diffusion kernel-smoothed continuous structural connectivity on cortical surface. *Imaging Neuroscience*, 3:IMAG-a.
- Yeo, B. T., Sabuncu, M. R., Vercauteren, T., Ayache, N., Fischl, B., and Golland, P. (2009). Spherical demons: fast diffeomorphic landmark-free surface registration. *IEEE Transactions on Medical Imaging*, 29(3):650–668.
- Zhang, F., Daducci, A., He, Y., Schiavi, S., Seguin, C., Smith, R. E., Yeh, C.-H., Zhao, T., and O’Donnell, L. J. (2022). Quantitative mapping of the brain’s structural connectivity using diffusion mri tractography: A review. *Neuroimage*, 249:118870.
- Zhang, T., Zhu, D., Jiang, X., Zhang, S., Kou, Z., Guo, L., and Liu, T. (2016). Group-wise consistent cortical parcellation based on connectonal profiles. *Medical image analysis*, 32:32–45.
- Zhao, F., Wu, Z., Wang, F., Lin, W., Xia, S., Shen, D., Wang, L., and Li, G. (2021). S3reg: superfast spherical surface registration based on deep learning. *IEEE transactions on medical imaging*, 40(8):1964–1976.
- Zhou, Z., Li, J., Williams, J., Fischl, B., and Aganj, I. (2026). Deep-learning cortical registration guided by structural and diffusion mri and connectivity. *bioRxiv*, pages 2025–10.

Appendix A. Gradient Computation

The gradient of the energy function H in (4), denoted by ∇H , is derived in the Supplement of Cole et al. (2025). Let $\{b_i\}_{i \geq 1}$ be an orthonormal basis of the tangent space $T_{\gamma_{id}}(\Gamma_\Omega)$ at γ_{id} . Then ∇H can be approximated by a truncated expansion using the first M basis elements:

$$\nabla H \approx \sum_{i=1}^M (\nabla_{b_i} H) b_i. \quad (\text{A1})$$

Now consider $\Omega = \mathbb{S}_1^2 \cup \mathbb{S}_2^2$, where the two spheres represent the left and right hemispheres. The diffeomorphism γ is defined componentwise as

$$\gamma(x) = \begin{cases} \gamma^1(x) & \text{if } x \in \mathbb{S}_1^2, \\ \gamma^2(x) & \text{if } x \in \mathbb{S}_2^2. \end{cases} \quad (\text{A2})$$

The directional derivative of the cost function H with respect to γ^1 in the direction $b_i \in T_{\gamma_{id}^1}(\Gamma_{\mathbb{S}_1^2})$ is given by

$$\begin{aligned} \nabla_{b_i} H_{\gamma^1} &= \int_{x \in \mathbb{S}_1^2} \int_{y \in \mathbb{S}_2^2} \{q_1(x, y) - q_2(x, y)\} \\ &\quad \times \left\{ \left[\frac{\partial q_2(x, y)}{\partial x} \quad \frac{\partial q_2(x, y)}{\partial y} \right] \begin{bmatrix} b_i(x) \\ b_i(y) \end{bmatrix} + \frac{q_2(x, y)}{2} (\nabla \cdot b_i(x) + \nabla \cdot b_i(y)) \right\} dx dy \\ &+ \int_{x \in \mathbb{S}_1^2} \int_{v \in \mathbb{S}_2^2} \{q_1(x, v) - q_2(x, v)\} \\ &\quad \times \left\{ \frac{\partial q_2(x, v)}{\partial x} b_i(x) + q_2(x, v) \nabla \cdot b_i(x) \right\} dx dv. \end{aligned} \quad (\text{A3})$$

Appendix B. Kernel Density Estimation

The truncated spherical heat kernel used in (1) is defined as

$$K_\sigma(x, y) = \sum_{l=0}^H (2l+1) e^{-l(l+1)\sigma} P_l(x \cdot y), \quad (\text{A4})$$

where $x \cdot y = \cos \theta$ is the cosine of the geodesic angle between x and y on the sphere, and P_l denotes the Legendre polynomial of degree l . The bandwidth parameter $\sigma > 0$ controls the amount of diffusion, with larger σ leading to greater smoothing through stronger attenuation of higher-frequency components via the factor $e^{-l(l+1)\sigma}$. The exact heat kernel is given by an infinite series; in practice, we truncate the expansion at $l = H$ for computational efficiency. This truncation is justified because the higher-order terms decay exponentially fast with l .

In the implementation, the kernel is first evaluated using the truncated spherical harmonic expansion. Entries corresponding to pairs with cosine similarity below a numerically determined threshold are then set to zero, resulting in a sparse kernel matrix. Equivalently, pairs of points whose geodesic distance exceeds a certain threshold—beyond which the kernel value is negligible—are ignored. This sparsification significantly reduces both computational cost and memory usage in subsequent matrix operations.

Note that applying a hard cutoff to the cosine similarity can make the numerical kernel approximation discontinuous in practice. However, this discontinuity is negligible when the cutoff threshold is chosen such that the kernel value at the truncation boundary falls below a prescribed numerical tolerance.

One advantage of the spherical heat kernel over the geodesic Gaussian kernel (Seguin et al., 2022) is its spectral representation. From (A4), the bandwidth parameter σ appears only in the scalar weights $e^{-l(l+1)\sigma}$, while the geometric terms $P_l(x \cdot y)$ are independent of σ .

As a result, when evaluating the KDE for multiple values of σ , one can precompute the Legendre components $P_l(x \cdot y)$ once, and then update the kernel efficiently by rescaling each harmonic term via $e^{-l(l+1)\sigma}$. This avoids recomputing pairwise geodesic distances or kernel evaluations for each σ , and reduces the computation to simple weighted sums (or matrix multiplications in the discrete setting), leading to substantially improved computational efficiency.

Appendix C. MMD Coefficient for Major Fiber Tracts

The MMD coefficient measures the difference between two sample sets at the distribution level, capturing discrepancies in endpoint distributions rather than at the edge level. A lower MMD coefficient indicates that the two point clouds have more similar distributions. Figure 5 shows that our endpoint-based method has a stronger ability to align the endpoints of major fiber bundles when viewed as point clouds.

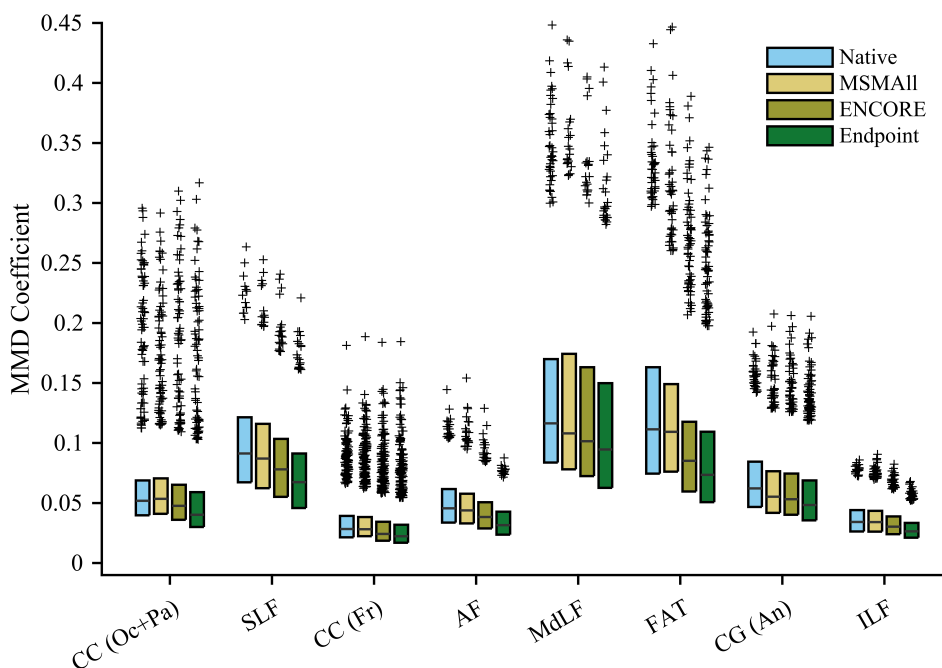


Figure A1. MMD coefficient for eight major fiber bundles.

Appendix D. Additional Analysis

Figure A2 illustrates the ground-truth warping used in the robustness experiment described in Section 5.2.

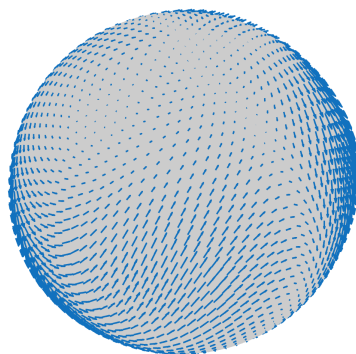


Figure A2. Ground-truth warping field used in the robustness experiment, visualized on an icosphere-4 mesh (2562 vertices).